Assessment of structural integrity of subsea wellhead system: analytical and numerical study

A.R. Maligno
Institute for Innovation in Sustainable Engineering, University of Derby, Quaker Way, DE1 3HD Derby (UK)
a.maligno@derby.ac.uk

R. Citarella
Department of Industrial Engineering, University of Salerno, Salerno (Italy)

V.V. Silberschmidt
Wolfson School of Mechanical and Manufacturing Engineering, Loughborough University, Loughborough (UK)

C. Soutis
School of Mechanical, Aerospace and Civil Engineering, University of Manchester, Manchester (UK)

ABSTRACT. Subsea wellhead systems exposed to severe fatigue loading are becoming increasingly a significant problem in offshore drilling operations due to their applications in wells with higher levels of pressure and temperature, situated at larger depths and in harsher environments. This has led to a substantial increase in the weight and size of offshore equipment, which, in combination with different loading conditions related to the environmental factors acting on the vessel and riser, has greatly increased the loads acting on subsea well systems. In particular, severe fatigue loading acting on the subsea wellhead system was detected. For this reason, a combined analytical and numerical study investigating the critical effect of crack depth on the overall structural integrity of subsea wellhead systems under cyclic loading was carried out. The study is based on a Linear Elastic Fracture Mechanics (LEFM) approach.

KEYWORDS. Fatigue crack growth; Zencrack; Defect assessment; Girth welds; Steel pipelines.

INTRODUCTION

Nowadays, offshore oil and gas exploration move into deeper waters and harsher environments. Technological advancements have enabled exploitation of previously inaccessible reservoirs, thanks to such important advancements as the improved ability to find offshore reservoirs and the capacity to drill deviated wells [1, 2]. Simultaneously, new technology makes extraction of more hydrocarbons and gas from existing wells possible, and many of them are now more than twenty years old. At the same time, economic demands imply a prolonged use of the existing welds. Therefore, subsea wells that are used for longer periods are likely to experience dangerous levels of accumulated load cycles. As a result, regulatory bodies are seeking assurances that the well-system conditions and integrity are being

correctly supervised, particularly with regard to fatigue, fail-safe design as well as analytical and numerical methodologies for their prediction [1-6]. Circumferential girth welds are a critical location for the structural integrity of pipelines and risers, and are produced using mechanised welding processes. Welding involves the heating of metal to its melting temperature followed by rapid cooling. As the weld metal cools it contracts, and the cooling rate influences a type of microstructure [7-10], mechanical properties [11,12] and a level of residual stresses [13] in the welds. Besides, flaws are likely to occur during the welding process. Fracture mechanics-based structural integrity assessments, most commonly referred to as either engineering critical assessments (ECAs) or Fitness-For-Service (FFS) assessments have found widespread acceptance to deal with such problems over the years [1-6]. The nuclear and offshore oil and gas industries are the main drivers behind the development of formal FFS procedures. Structural integrity assessments [14, 15] can be used at the design stage, to estimate the maximum flaw size that will not grow to intolerable levels during the life of the component, or to assess defects grown after some time in service. Such information about defect tolerance relies on the availability of representative and reliable experimental data, on which any defect-assessment calculation is based. This study aims at developing a fracture mechanics-based model to study and elucidate the effects linked to crack depth and shape as well as crack propagation in the subsea wellhead systems under cyclic loading conditions. In particular, this research focuses at simulations of crack propagation in a conductor/casing pipe girth welds and at understanding the impact of flaws on the drift-off/drive-off capacities and on the residual fatigue life of the wellhead system. In order to determine the maximum allowable flaw size and to simulate crack propagation under cyclic loading, the in-house software Zencrack was used. The validity of this software has been widely assessed in several research and industrial projects [16, 17]. The wellhead system was calibrated to fit the *S-N* curve of *Quality Category* Q2 as described in BS 7910 Code [18], which is equivalent to BS 7608 Code design class E [19].

WELLHEAD SYSTEM

A typical configuration of a wellhead system is shown in Fig. 1. In this study, a simple two-pipe wellhead system comprising a conductor pipe (diameter 36". thickness 1.5") and a surface casing pipe (diameter 22", thickness 1.0"), with a rigid lock wellhead, was considered. The girth weld for both the conductor and casing pipes to be investigated is class E type following BS7910 code. The effect of stress concentration or misalignment was not considered in this study. Both the conductor and the casing are considered fixed at the base, and a constant-amplitude cyclic bending moment was applied at the top end, with a crack plane situated half way along the length (Fig. 2).

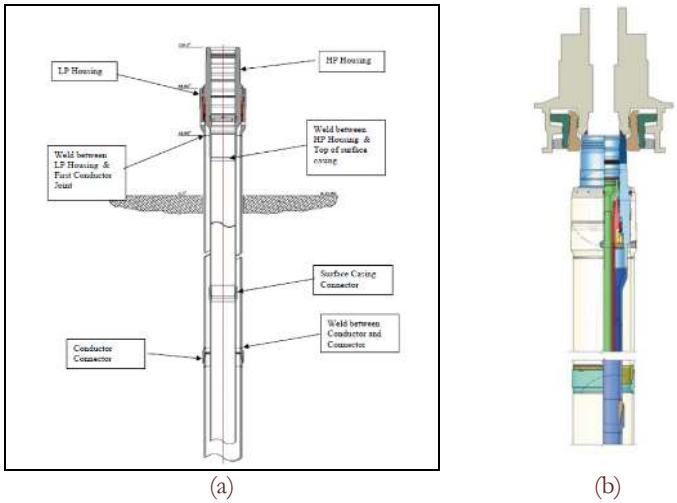

(a) (b)

Figure 1: Typical wellhead system: (a) schematic presentation [5]; (b) detail.

No presence of cement in the annular spacing between the conductor and the casing pipe or the surrounding soil was assumed. The crack geometries and the applied load, used in this study, are symmetric with respect to the YZ plane (Fig. 2). Hence, it was proposed to use half models for all analyses taking advantage of this symmetry. Material properties for X80 steel used for the casing and X65 steel for the conductor are summarised in Tab. 1.

	X80 steel (Casing)	***X65 steel (Conductor)***
Young's modulus [GPa]	210	
Poisson ratio (μ)	0.3	
Yield stress [MPa]	550	448
Fracture Toughness (K_{IC})	7115 MPa√mm (225 MPa√m)	

Table1: Material properties.

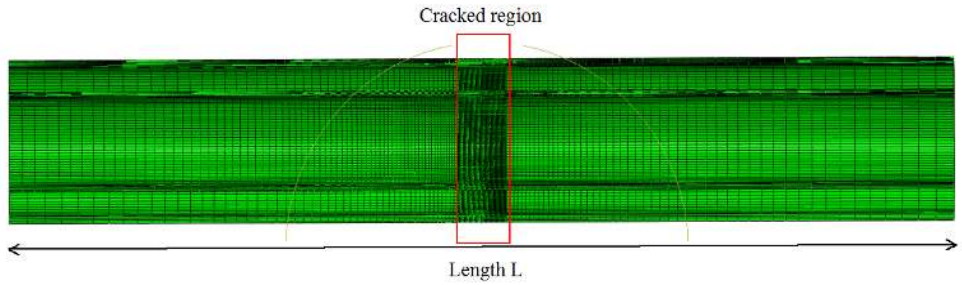

(a)

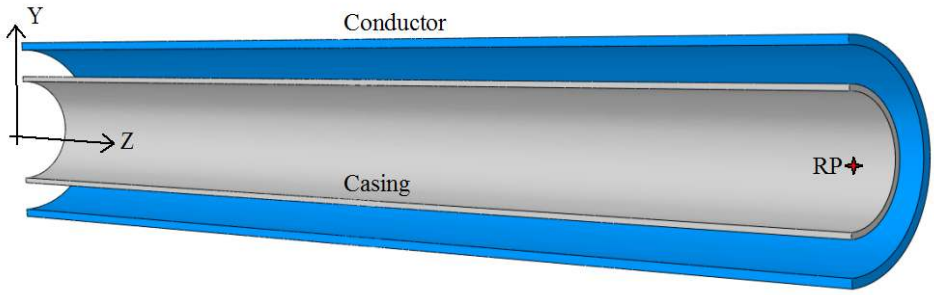

(b)

Figure 2: Numerical model of wellhead system: (a) full-system (A refined mesh was used in the cracked region; the crack is placed at L/2); (b) cross section of conductor/casing system in this study.

Loading and Boundary Conditions

The applied load is a bending moment at the reference point (RP), shown in Fig. 2, which corresponds to a cyclic stress with a magnitude of 1 MPa (R=-1) on the outer surface of the conductor pipe. This is then scaled to get the required stress value, when needed. The initial study was based on the stress value of 80 MPa at the outer face of the conductor pipe. In the finite-element model, two loading surfaces are "constrained" together to the RP via kinematic coupling. The boundary conditions are described with the help of Fig. 2:

- The bending moment was applied to RP (reference point) and via a kinematic coupling constraint to nodes on the remote end face at Z = L.
- The conductor and casing were constrained to undergo zero displacements at Z = 0.

Boundary Conditions: Kinematic vs Distributing Coupling

A separate study was performed to check the adequacy of this coupling compared to the distributed boundary conditions. Kinematic coupling was enforced in a strict master-slave approach [20]. Degrees of freedom (DOFs) at the coupling nodes were eliminated, and the coupling nodes were constrained to move with the rigid-body motion of the reference node. Generally, kinematic coupling constraint does not allow relative motion among the constrained DOFs, while allowing relative motion of the unconstrained ones.Distributing coupling was enforced in an average sense [20]. DOFs at the coupling nodes were not eliminated. Rather, the constraint was enforced by distributing loads such that the resultants of the forces at the coupling nodes were equivalent to the forces and moments at the reference node, and force and moment equilibrium of the distributed loads about the reference point was maintained. A distributing coupling allows relative motion of the constrained and unconstrained DOFs. The effect of these two different coupling constraints should be evaluated during the crack propagation in the conductor and casing as depicted in Fig. 3. The kinematic coupling

provides conditions that are more realistic for the case with parallel surfaces in the region, in which the bending moment is applied. For this reason this constraint was preferred to the distributing coupling, which allows more freedom to the displacements in the loaded section.

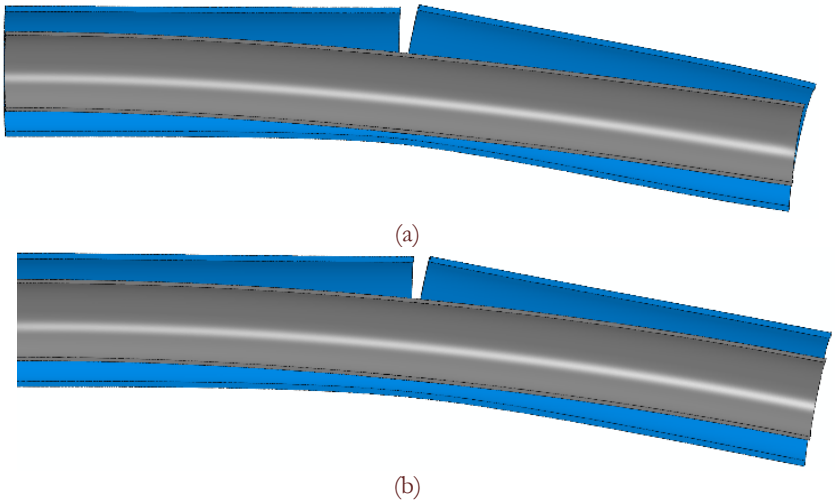

(a)

(b)

Figure 3: Effect of distributing (a) and kinematic (b) couplings.

PRELIMINARY STUDY

A LEFM-based methodology, which adopted a Paris-crack propagation law, was developed to calculate the crack growth rate and perform initial crack-size calibration exercise for the conductor and the casing considered separately. In order to achieve a close match between the residual life, based on the Paris law, and the fatigue life, based on the weld *S-N* curves (E class type [18]) in the conductor pipe, the following iterative procedure was implemented:

- Determination of initial crack size for the calibration exercise.
- Determination of crack-growth data for the appropriate material in a seawater environment (-1100 mV cathodic protection).
- Analytical crack-growth analysis for different stress ranges.
- Crack-growth analysis from the initial crack to the failure condition using Zencrack.
- Comparison of preliminary numerical and analytical data.
- Re-adjustment of the initial crack size depending upon the results of the analysis.

The outcome of this activity was the determination of the Paris-law data and the initial crack size to be applied in subsequent crack modelling of the conductor/casing system. It is paramount to emphasise that FE simulations were based on linear elastic fracture mechanics with the values of stress intensity factor (SIF) *K* calculated employing the *J* contour integral [21-22]. SIFs were calculated at multiple points along the crack [16, 17]. The *failure condition* was assumed to occur when the crack either grows through the wall thickness (and reaches the opposite surface) or reaches an unstable crack size (critical *K*) under the applied cyclic loading.

Analytical Evaluation of Stress Intensity Factor K_I

An analytical expression was derived to estimate the stress intensity factor as a function of crack depth. This was subsequently used to estimate the initial crack size for the finite-element calibration analysis.

A number of available publications [18, 23] were considered to evaluate analytically the stress intensity factors at the deepest point of an elliptical crack located circumferentially on the inner wall of a cylinder as shown in Fig. 4.

The procedure described in BS 7910 [18] using Eq. 1 for the evaluation of SIFs was found to give non-reliable results due to an error in the value of the term $(Y\sigma)$ as prescribed in the equation M24 of the Annex M of BS 7910:

$$K_I = (Y\sigma)\sqrt{\pi a} \tag{1}$$

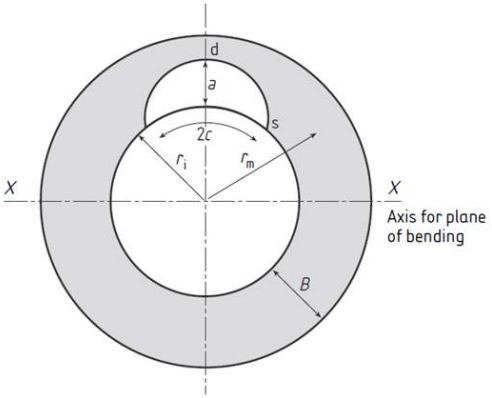

Figure 4: Surface flaw of internal cylinder.

This error was possibly due to a mistake in equation M24 for the contribution of stress due to the global bending moment. It was therefore decided to use the procedures described in the publication, "Stress Intensity Factor and Limit Load Handbook" edited by British Energy Generation Ltd [23]. The equation used to calculate the SIFs at the deepest point of the elliptical crack is:

$$K_I = \sqrt{\pi a}\left(\sum_{i=0}^{3}\sigma_i f_i\left(\frac{a}{B},\frac{2c}{a},\frac{r_i}{B}\right)+\sigma_{bg} f_{bg}\left(\frac{a}{B},\frac{2c}{a},\frac{r_i}{B}\right)\right) \tag{2}$$

The sizes considered for the cylinder (conductor pipe) are:

- outer radius r_o = 18";
- wall thickness (B) = 1.5";
- internal radius r_i = 16.5";
- the dimensions of the planar circumferential elliptical crack on the inner wall of the cylinder are $a$and $2c$, where a is the depth and $2c$ the length measured at the inner radius (Fig. 4).

The values of the coefficient f_{bg} used in the analytical evaluation of the SIFs and the calculated values of SIFs are given in Tab. 2. The term σ_{bg} in Eq. 2 is defined as the maximum outer-fibre bending stress. The SIF values have been determined for the following ratios a/B: 0.01 (~0.0); 0.2; 0.4; 0.6 and 0.8.

The tabulated coefficients for Eq. 2 are provided in [23]. The (mode-I) stress intensity factor at the deepest point of the crack has been calculated for the following ratio between the crack depth a and half-arc length c:

$a/c = 1$

This ratio is assumed to remain constant throughout the analytical calculation. This assumption was considered acceptable in the preliminary calibration study. Since in this study only bending stresses are taken into account, Eq. 2 can be simplified as follows:

$$K_I = \sqrt{\pi a}\left(\sigma_{bg} f_{bg}\left(\frac{a}{B},\frac{2c}{a},\frac{r_i}{B}\right)\right) \tag{3}$$

SIFs in Tab. 2 are given for *unit* outer fibre stress. The trend of the stress intensity factor K_I is shown in Fig. 5.

a/B	a [mm]	a/c	f_{bg}	K_I Bending stress 1 MPa
0.01	0.381	1.0	0.599	0.655
0.2	7.62	1.0	0.613	2.999
0.4	15.24	1.0	0.636	4.401
0.6	22.86	1.0	0.659	5.585
0.8	30.48	1.0	0.685	6.703

Table 2: Coefficients f_{bg} and SIFs for a range of crack sizes.

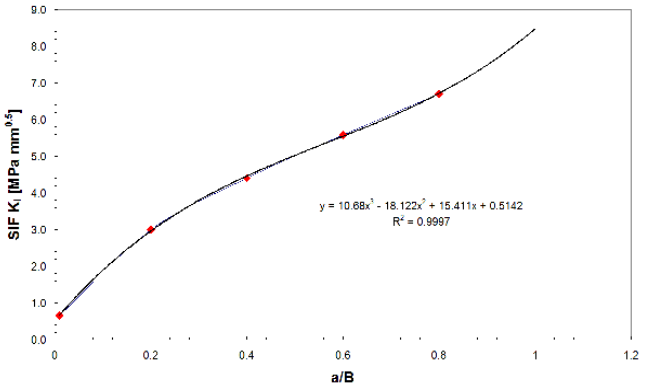

Figure 5: Trend of K_I *vs.* a/B for deepest point of conductor's crack.

Using the curve fitting techniques, a curve was fitted through the tabulated values for a/B, on the X-axis, and SIFs, related to the maximum fibre stress of 1 MPa, on Y-axis, as shown in Fig. 5. The polynomial equation representing this curve is:

$$K_I = 10.68(a/B)^3 - 18.122(a/B)^2 + 15.411(a/B) + 0.5142 \quad (4)$$

This equation was used to perform analytic crack-propagation calculations to estimate the initial crack size.

Finite-element strategy

After the preliminary analysis, a finite-element (FE) model was developed to evaluate the residual life of the pipe system under study with an initial semi-circular crack. The details of the numerical model used for the crack growth FE analyses are shown in Fig.6.

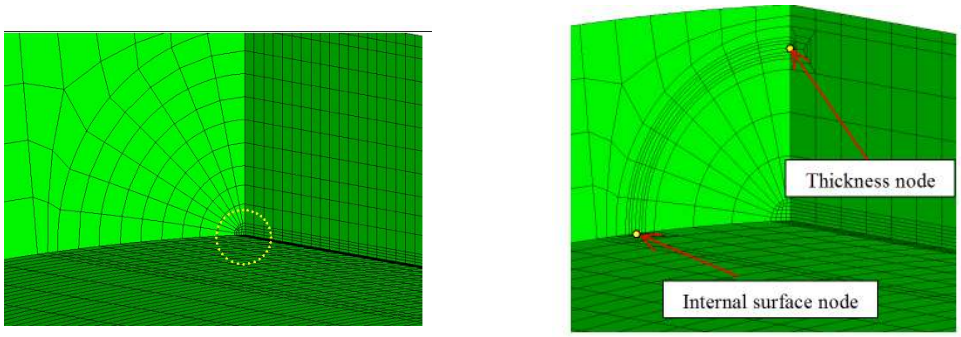

Figure 6: FE model used in the crack propagation analysis: (a) mesh without crack; (b) mesh with crack and position of nodes of interest. The Thickness node will degenerate into the External Surface node while reaching the external surface.

The elements used were full-integration *20*-node hexahedral elements. In the model with the crack, Zencrack introduced the crack details by replacement of a line of eight elements with crack blocks, resulting in the FE model of the cracked pipe. The mesh of the crack so created was a focussed mesh, consisting of quarter-point crack-tip elements along the crack front with $r^{-1/2}$ singularity. The number of elements in the FE models with the crack and without it (conductor and casing separately considered) was never less than 135000. The node lying on the outer radius is referred to as *external surface node*, the node on the inner radius as *internal surface node* and the node on the wall thickness as *thickness node* (Fig. 6b).

Estimation of Initial Crack Size for S-N Relation

A comparison of the stress intensity factors, evaluated at the deepest crack-front point, for different initial crack configurations, is presented in Tab.3. As demonstrated in Tab. 3, the analytical and numerical values show excellent agreement and confirm that this type of meshing is suitable for crack-growth predictions. The maximum discrepancy in these results is equal to nearly 1.7% (for $a/B = 0.8$).

a/B	K_I (Analytical solution) Bending stress 1 MPa	K_I (FE solution) Bending stress 1 MPa
0.2	2.999	2.981
0.4	4.401	4.364
0.6	5.585	5.522
0.8	6.703	6.592

Table 3: Comparison of K_I for analytical and numerical solutions.

In this section, the initial crack size and material coefficients of the Paris crack-growth law were evaluated and calibrated against the *Quality Category 2* (Q2) *S-N* curve as given in BS 7910 Code.
In order to evaluate the residual life, the Paris equation was used:

$$\frac{da}{dN} = A(\Delta K)^m \tag{5}$$

where the coefficients A and m for the steel under analysis are:
$A = 5.21\text{x}10^{-13}$; $m = 3$ for da/dN in mm/cycle and ΔK in MPa $\text{mm}^{1/2}$.

Minimum crack size

The size of the elliptical initial crack on the inner wall of the pipe was also estimated. It was of paramount importance that the estimated number of cycles for each crack size, at different stress range levels, was reasonably close to the fatigue cycles of the Q2 *S-N* curve. In BS 7910 Code, the quality categories refer to particular fatigue design requirements or to the actual fatigue strength of *flaw-containing* components. The quality categories are defined in terms of the ten *S-N* curves labelled Q1 to Q10. These are described by the following equation [18]:

$$\Delta\sigma^3 = constant \tag{6}$$

The value of such constant for the *Quality Category 2* (Q2) for steel is: 1.04×10^{12} cycles.
At a stress range of 80 MPa, the estimated life is 2×10^6 for X80 steel. This reference stress and the number of fatigue life cycles were used in the first iterative calculations. The numerical integration of the Paris law (Eq. 5) was carried out using a fixed increment *da*. After each increment of crack advance an average number of life cycles was determined as

$$dN_{i+1} = \sum \frac{1}{2}\left(\frac{da}{(da/dN)_{i+1}} + \frac{da}{(da/dN)_i} \right) \tag{7}$$

The total life is therefore:

$$N_{i+1} = N_i + dN_{i+1} \tag{8}$$

The SIFs were calculated using the fitted curve described by Eq. 1 for various a/B values. After a number of iterations the evaluated crack depth a that gave a residual life estimate of 2×10^6 cycles at the reference stress range of 80 MPa was 3.92 mm.
A comparison of cycle estimations at various stress ranges, namely, 300 MPa, 80 MPa, 50 MPa, 20 MPa, and at different initial crack sizes a (3.81 mm, 7.62 mm, 3.92 mm) is shown in Fig. 7. The values 3.81 mm and 7.62 mm were chosen as they represent a/B=0.1 and 0.2. The initial crack size of 3.92 mm matches the *S-N* curve for all the stress ranges considered and, therefore, it was used for the preliminary finite-element analyses of crack growth.
During this analytical study, the SIFs were constantly monitored and checked against the fracture toughness (K_{IC}) value for X80 steel (225 MPa$\sqrt{\text{m}}$) to detect any failure due to fracture. The analytical solution showed that the stress intensity factor during the crack propagation did not exceed the K_{IC} value; failure was achieved due to the break-through condition.

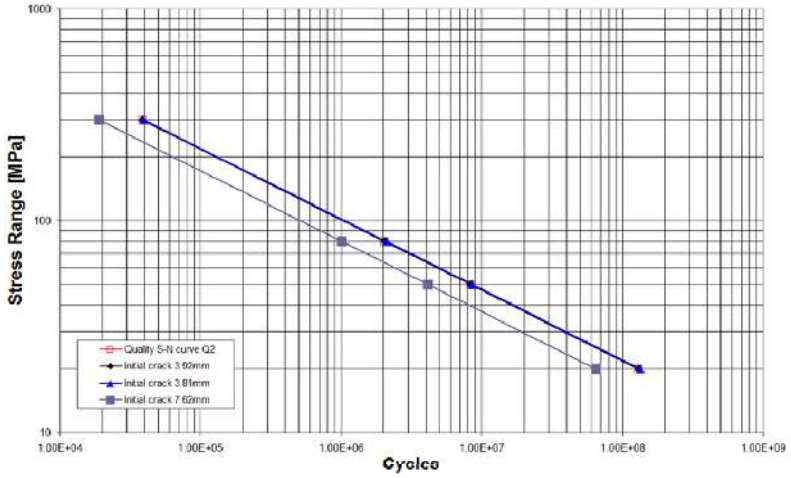

Figure 7: Life at different crack sizes and stress ranges.

FE Results: Conductor

The results obtained from the numerical analyses with the initial crack length equal to 3.92 mm (maximum crack depth) and the stress range of 80 MPa are shown in Fig. 8 and Fig.9.

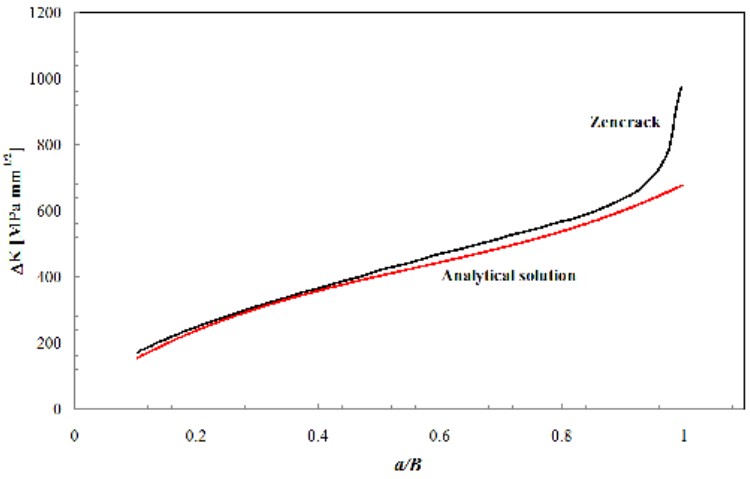

Figure 8: Comparison between FE and analytical SIFs for initial crack length 3.92 mm (K_{IC}= 7115 MPa√mm).

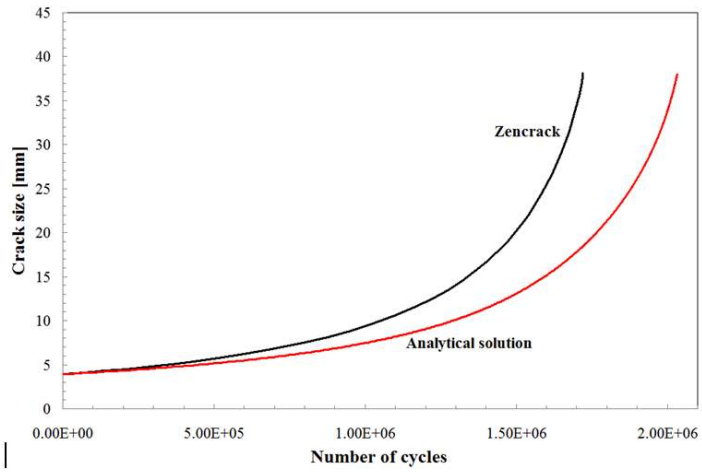

Figure 9: Comparison between analytical and FE residual life estimation for initial crack length 3.92 mm.

The estimated residual life (i.e. the number of cycles for the crack to grow to the specific length) evaluated by Zencrack was 1.72×10^6 cycles whereas the analytical calculations gave a residual life of 2.03×10^6 cycles, with a difference of nearly 15%. This discrepancy between the analytical solution and the FE-based solution (with Zencrack) was likely due to the following factors:

- $r_i/B = 11$ is slightly out of the valid range of 10 (as given in the reference);
- the analytical solution assumes that the shape of the crack remains constant, i.e the ratio $a/c = 1$, whereas in the FE simulation the crack shape would take a more natural shape, based on the energy release rate at each crack-front node.

In order to get the residual life closer to the target value of 2.03×10^6 cycles it was decided to assess a more suitable initial crack size using Zencrack. The analytical study suggested an increase of about 17% in the crack dimensions to achieve the fatigue life of 1.72×10^6 cycles. Therefore, the size of the initial crack was modified to 4.74mm.
Fig. 10 shows the results of the analytical calculations with initial crack size equal to 4.74 mm: with such an assumption, the analytical assessment matches exactly the Zencrack results calculated with an initial crack size equal to 3.92 mm. It was therefore decided to assume an initial crack size $a = 3.1$ mm (i.e.: 3.92 - 0.82) in the FE analyses.

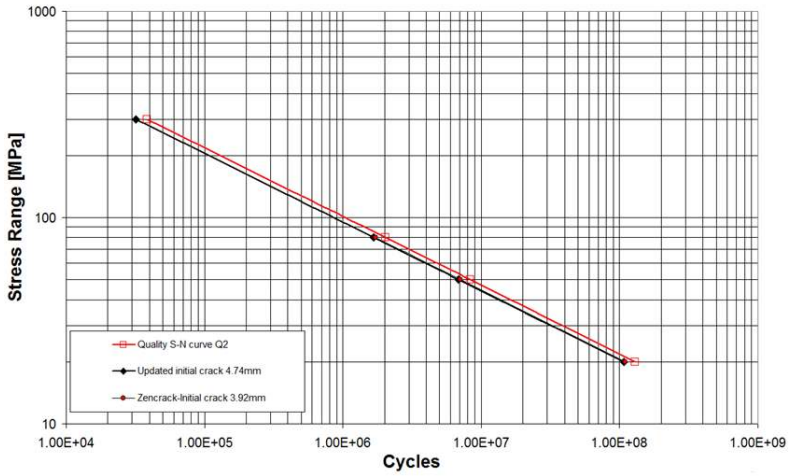

Figure 10: Determination of new crack size. The initial a=3.92 mm was increased to a = 4.74 mm in the analytical calculation to match Zencrack results.

Results of the numerical analysis for the crack size a = 3.1 mm (stress range 80 MPa) presented in Fig. 11 show that the residual life achieved for this crack size is very close to the target value of 2.03×10^6 cycles. This figure also presents a plot of the results of a Zencrack analysis, in which the crack shape was ***forced*** to maintain the rato $a/c = 1$ as the crack propagated through the wall thickness. This plot demonstrates that there is a tangible effect of the crack-front shape evolution.

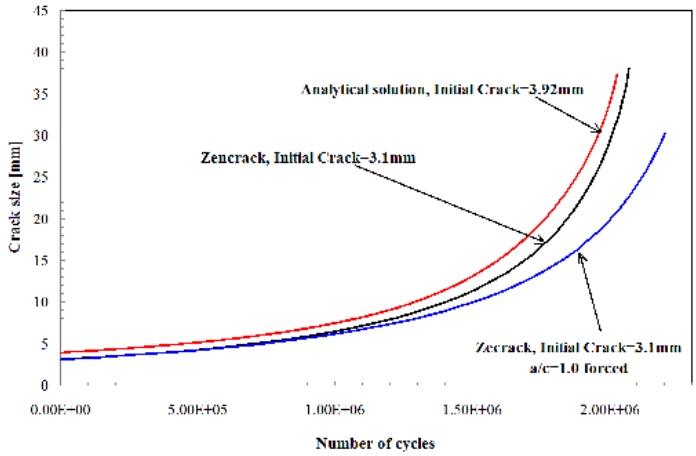

Figure 11: Comparison of analytical and numerical residual life (target=2.0x10^6 cycles)

FE Results: Casing

The same methodology described in Section 3.2 was used to evaluate the minimum size of an elliptical surface crack on the inner wall of the casing tube. Therefore, by means of the stress intensity factor K_I, calculated analytically for different stress ranges and crack sizes, the number of fatigue cycles was evaluated and compared with the levels of the *S-N* curve of *Quality Category* 2 in Code BS7910. This iterative process was carried out until a close match was found. Using the K_I values for different a/B ratios from the analytical solution, a polynomial curve

$$K_I = 8.724(a/B)^3 - 14.796(a/B)^2 + 12.583(a/B) + 0.4198 \quad (9)$$

was fitted.

The minimum value of a evaluated analytically was 3.18 mm, and the number of fatigue cycles evaluated under the reference stress range of 80 MPa was nearly equal to 2.03×10^6. In order to achieve the fatigue life closer to 2.03×10^6 cycles, further iterations were carried out using Zencrack software to determine the minimum crack size. As described in Section 3.2.3, the finite-element model of the casing pipe was developed to evaluate the residual life based on fracture mechanics and using the Paris growth law with material parameters, $A = 5.21\times10^{-13}$ and $m=3$.

Crack-propagation analyses with the initial elliptical (semi-circular) crack with a (minor-axis) values of 3.184 mm and 2.873 mm were carried out and the number of fatigue cycles compared with the *S-N* curve (Tab. 4 and 5).

Stress range	Cycles (*S-N* curves)	Cycles (FE solution)
300	3.852E+04	3.4968E+04
80	2.031E+06	1.8440E+06
50	8.320E+06	7.5530E+06
20	1.300E+08	1.1802E+08

Table 4: Comparison of *S-N* curve data and numerical results for 3.184 mm initial "calibration" crack

Stress range	Cycles (*S-N* curves)	Cycles (FE solution)
300	3.852E+04	3 .8172E+04
80	2.031E+06	2.0130E+06
50	8.320E+06	8.2452E+06
20	1.300E+08	1.2883E+08

Table 5: Comparison of *S-N* curve data and numerical results for 2.873 mm initial crack

In order to get the residual life closer to the target value of $2.03\text{x}10^6$ cycles, further FE analyses were carried out and the initial value of a = 2.839 mm was determined (Tab. 6).

Stress range	Cycles (*S-N* curves)	Cycles (FE solution)
300	3.852E+04	3.856E+04
80	2.031E+06	2.033E+06
50	8.320E+06	8.328E+06
20	1.300E+08	1.301E+08

Table 6: Comparison of *S-N* curve data and numerical results for 2.839 mm initial crack

The crack propagation profiles showing the elliptical crack (symmetrical model) growing from its initial size a = 2.839 mm to the outer wall of the pipe are shown in Fig. 12.

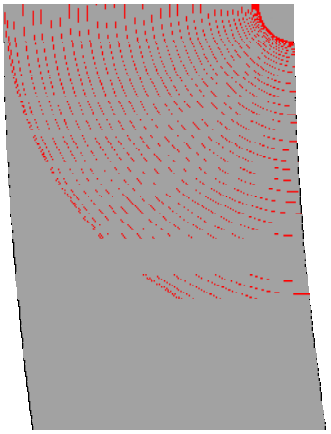

Figure 12: Detail of crack path.

FULL-SYSTEM STUDY

The undertaken preliminary crack-propagation analyses on the full model (combining the conductor and casing pipes), demonstrated that the crack in the conductor pipe grew much faster than that in the casing pipe. It was found that the inner-wall crack in the conductor pipe grew to become a through-wall-thickness crack and further, grew nearly 120° wide in the cross-section of the conductor pipe before the inside-wall elliptical crack in the Casing pipe showed any substantial growth. A three-stage crack-propagation strategy was therefore adopted to evaluate the cumulative fatigue life of the system and of the individual pipes.

Three-stage Analysis Strategy

The three stages of the used strategy are:

- Stage 1: Application of the fatigue cyclic load (bending moment) to the combined model with the initial elliptical cracks both in the casing and conductor pipes; then the crack in the conductor pipe was allowed to grow until it broke through the wall thickness.
- Stage2: Continuation of Stage-1, until the crack in the conductor stabilised.
- Stage 3: Continuation until the inner-wall crack in the casing pipe became a through-wall-thickness crack.

Stage1

Crack-propagation analysis in Stage 1 was performed on the combined conductor/casing system described above with initial semi-circular cracks in both pipes (Fig. 13).
The FE model and the location of the cracks are displayed in Fig. 14.

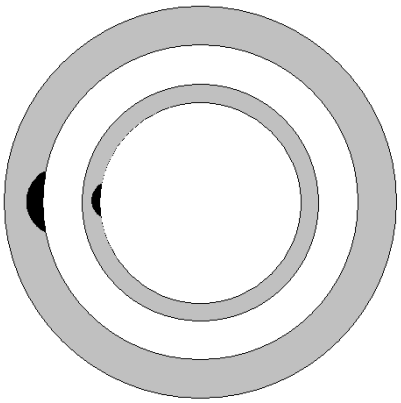

Figure 13: Stage-1 crack configuration.

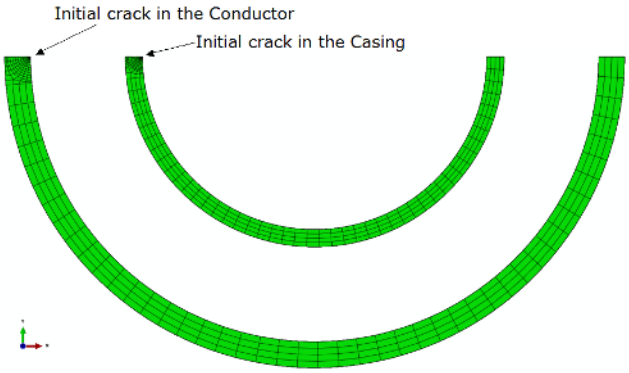

Figure 14: Location of initial cracks (half model)

Numerical Results: Stage 1

The final dimensions and shapes of simulated cracks in the conductor and in the casing, corresponding to the end of Stage 1, are shown in Fig. 15.

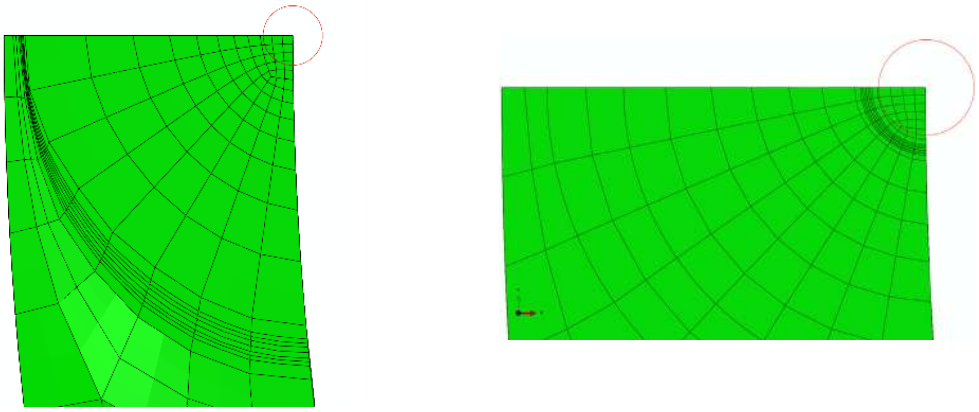

(a) (b)

Figure 15: Simulated final crack shape at the end of Stage 1 analysis: (a) conductor; (b) casing. The circle show the initial crack configuration.

It can be noticed that a negligible crack growth took place in the casing (Fig. 15b). The results, in terms of *a-n* and *K- a* relationships, for both the inner-surface crack-front node and the through-the-thickness crack-front node, at the end of Stage 1 (when the conductor pipes crack was about to break through the thickness) are presented in Figs. 16-18. The respective number of fatigue cycles *n* was 2.6E+06.

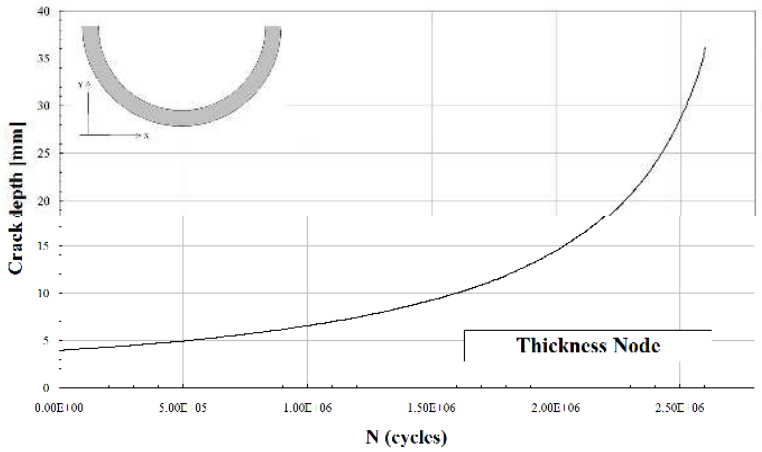

Figure 16: *a vs. N* for thickness node (conductor).

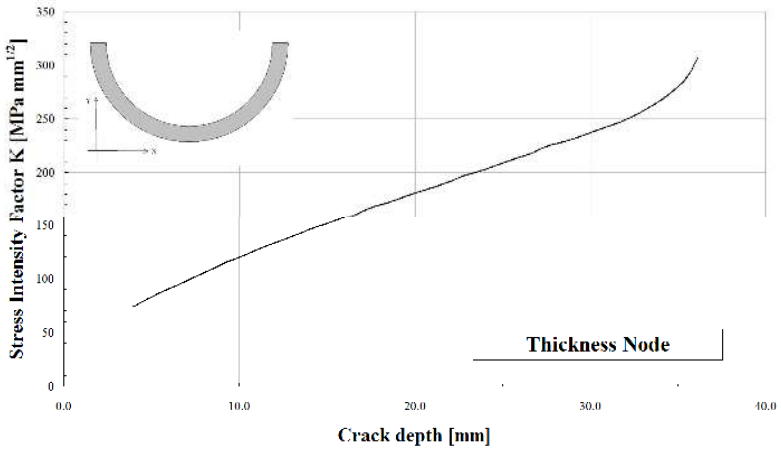

Figure 17: *K vs. a* for thickness node (conductor).

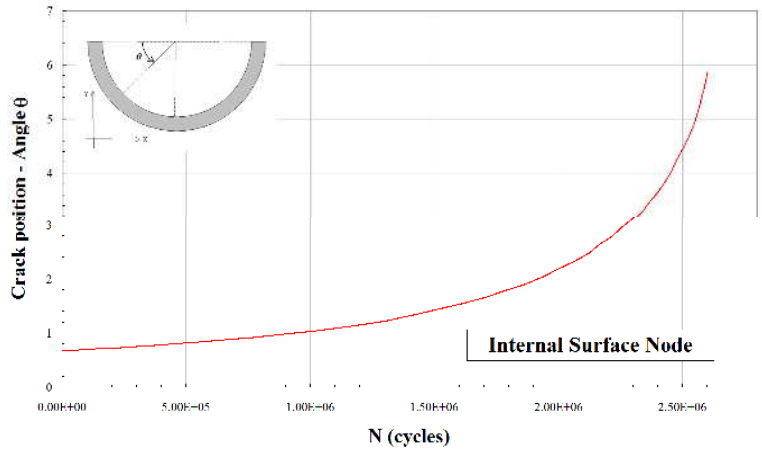

Figure 18: *a vs. N* for internal surface node (conductor).

Stage 2

The second stage of the analysis required an update of the crack shape in the conductor so that a *through-thickness* crack profile was created. The strategy to update a crack from a corner to through-the-thickness crack is described by Maligno *et al.* [16]. In Stage 2, the FE mesh of the conductor pipe, as obtained at the end of Stage-1 crack-growth analysis, was appropriately adjusted using a spline function for the new through-thickness crack front, as shown in Fig. 19.

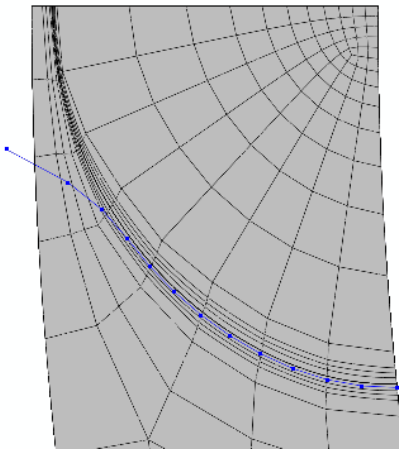

Figure 19: Spline (blue line) used to create through-the-wall crack.

While the crack in the conductor grew during the simulation, a severely distorted mesh was generated. The consequence of this was that, to further extend the crack growth, some "manual" interventions were required to update the crack profile. In this study, different crack profiles were introduced to understand thoroughly the consequences of flaw extension in the conductor. The used *through-the-thickness* crack profile was determined analytically [16]. However, in order to investigate the effect of particularly large flaws in the structural integrity of wellhead systems (arising from a combination of variable loading conditions and aggressive environmental effects), two additional hypothetical shapes were investigated. The studied crack profiles are labelled as described in Tab. 7:

Crack profiles	*Method of determination*
TW 1	analytical
TW 2	analytical
TW 3	analytical
TW 4	hypothetical
TW 5	hypothetical

Table 7: Crack-profile labels and estimation technique.

Starting from the front of the initial through-the-thickness crack *TW1* (Fig. 20a) the crack was extended in five steps up to a condition in which the remaining ligament of the conductor pipe was exposed only to compressive stresses [24, 25] so that any crack opening was prevented. Throughout these analyses, the crack growth in the inner wall of the casing pipe was found to be negligible. For this reason and for sake of clarity only the conductor pipe is shown in the figures.

Step 1

During this step (*TW1*), the crack grew up to reaching a configuration, where its front extended circumferentially for nearly 120° (Fig. 20b). At this crack extension, further propagation was prevented from further development due to severe distortion of the FE mesh (formation of inside-out elements) near the crack front. The initial and final crack sizes and crack extensions are summarised in Tab. 8:

	Conductor	*Casing*
Initial crack size [mm]	3.92	2.839
Crack extension (thickness) [mm]	36.13	3.68
Crack extension (internal surface) [mm]	42.14	3.75

Table 8: Characteristic crack dimensions at Stage 1.

Step 2

Maintaining the same position and shape of the crack front as provided at the end of Step 1, the FE mesh near it was smoothed and the simulation analysis restarted allowing the crack to grow to position *TW2* as depicted in Fig. 20c.

Step 3

The FE mesh at the crack front was modified as in Step 2, keeping the crack shape as calculated at the end of Step 2 to get further crack growth to position *TW3* (Fig. 20d).

Steps 4 and 5

Although no crack propagation was detected at the end of Step 3, due to highly compressive stresses, two further positions, *TW4* and *TW5* (Figs. 20e and f, respectively), were considered to estimate the capability of the conductor to bear loads in presence of extended flaws.

Numerical Results: Stage 2

Similarly to Stage 1, throughout Stage 2 propagation of the crack on the inner wall of the casing pipe was found to be negligible. Fig. 21 shows the variation of stress intensity factor *K* with growth of the through-the-thickness crack along the circumference of the conductor pipe. Apparently, *K* increased as the crack grew but once the crack front partially crossed

the compressive zone at the pipe's cross-section the stress intensity started dropping. This phenomenon was further studied and it is explained in *Analytical Study: Stage 2*.

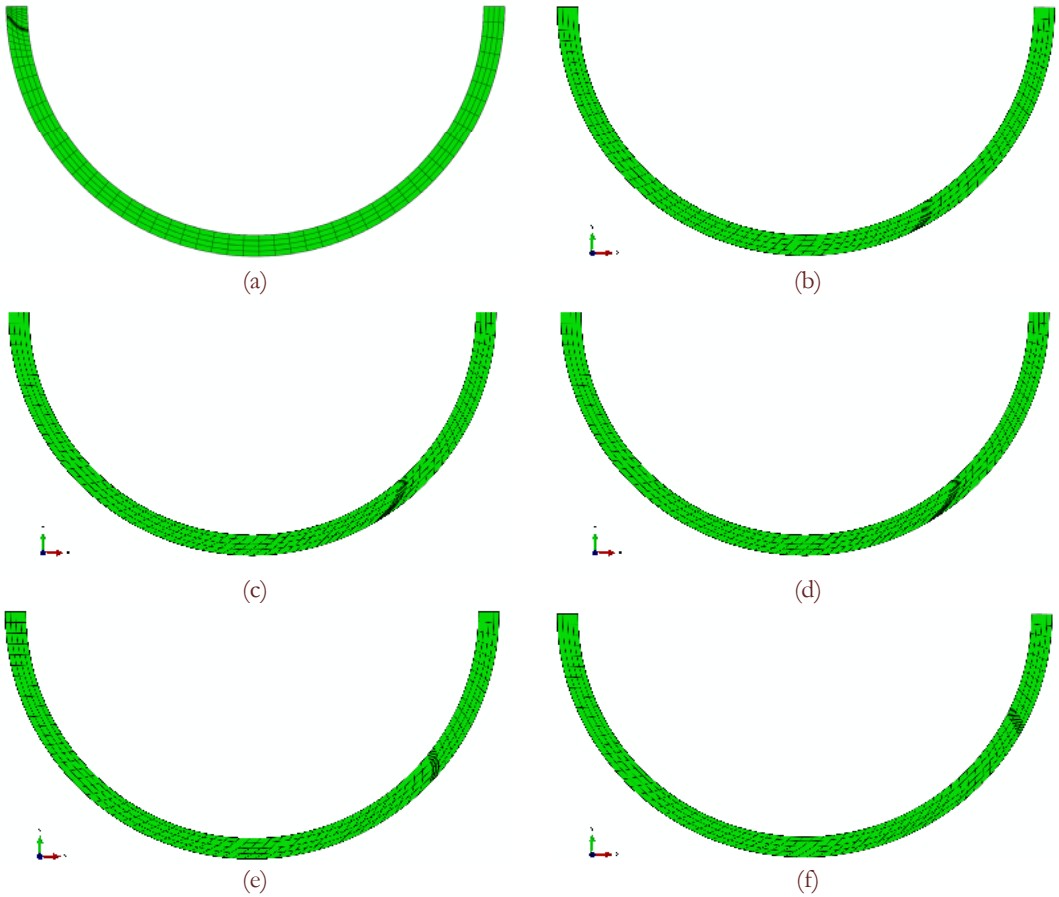

Figure 20: Multi-step procedure at Stage 2: (a) initial through-the-thickness crack; (b) crack configuration at end of Step 1 (TW 1); (c) crack configuration at end of Step 2 (TW 2); (d) crack configuration Step 3 (TW 3); (e) crack configuration Step 4 (TW 4); (f) crack configuration at Step 5 (TW 5).

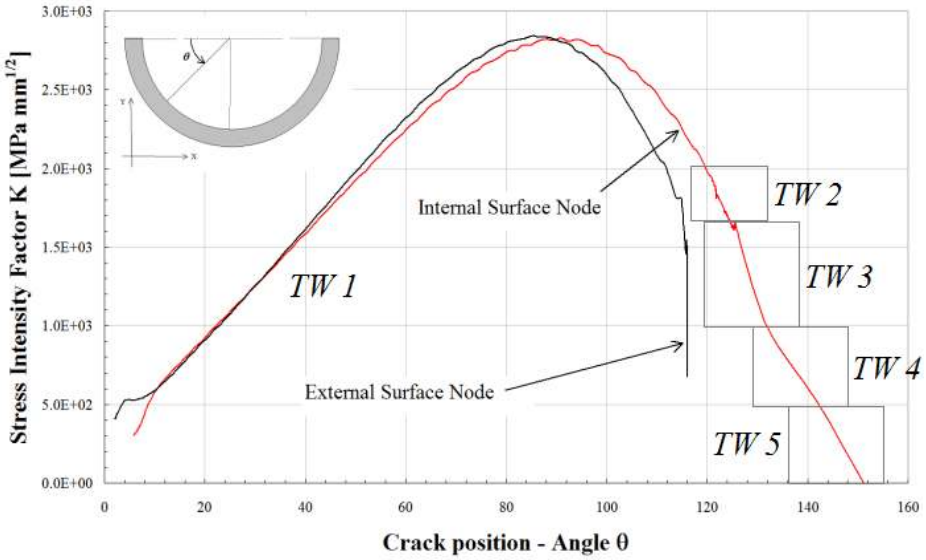

Figure 21: Comparison of overall K curves for internal and external surface nodes.

It is understandable that when the crack front approached some 90° on the circumference the crack front started changing its shape and elongated. The external node was likely to enter the compressive zone [24, 25], and the crack growth slowed down, whereas the internal node remained in the tensile-stress zone and continued to propagate (Fig. 22). The number of cycles was monitored for the whole set of crack configurations; the respective results are summarised in Tab. 9.

Crack Shape	*Cycles*
Corner Crack	2.600E+06 (to reach external surface)
TW 1	1.910E+05 (to reach configuration *TW 2*)
TW 2	1.450E+03 (to reach configuration *TW 3*)
TW 3	No growth
TW 4	No growth
TW 5	No growth
Total number of cycles	2.7925E+06

Table 9: Number of cycles for different crack configurations.

It is interesting to observe that at crack configuration *TW 3* the crack propagation can be considered ***stabilised*** and no subsequent crack propagation was detected. It is paramount to notice that, while the crack advanced, an **inversion** of the trend for the stress intensity factor occurred. The consequence of this particular behaviour can be attributed to the position of the crack in relation to the neutral axis, as also described in [24, 25]. In fact, the crack, at its initial stage, was entirely in tension (Fig. 22a), but when it advanced, the neutral axis changed its initial position; as soon as the crack position was between 85° (external surface) and 90° (internal surface), the crack started to be exposed to compressive stresses (Fig. 22b). In particular, from Fig. 22b it is possible to deduce that for the crack positions close to 110° the *K* value underwent an abrupt reduction. Therefore, the flaw in proximity of the external surface was totally under compressive stress and no crack propagation could be detected (according to the Linear Elastic Fracture Mechanics criteria).

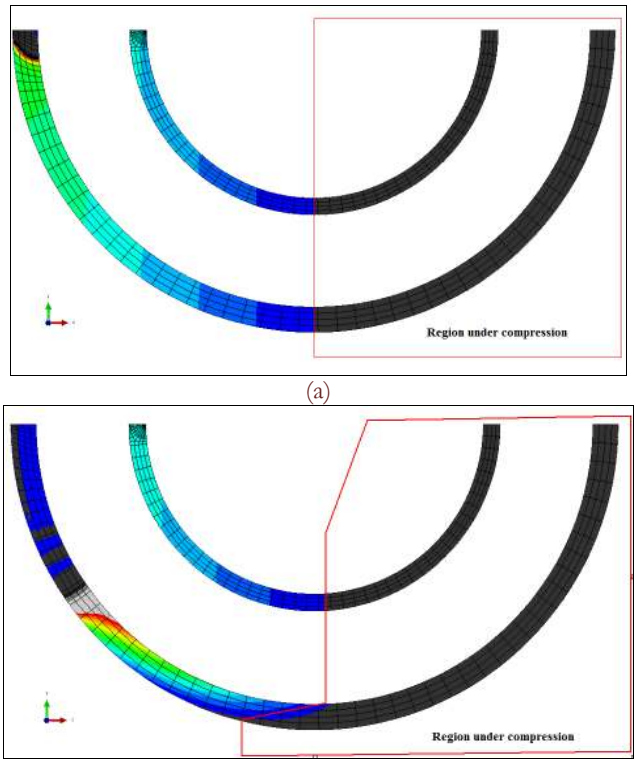

(a)

(b)

Figure 22: Crack configurations from FE analysis: (a) initial crack configuration; (b) extended crack configuration.

Analytical Study: Stage 2

In order to further investigate ***inversion*** of the trend of the stress–intensity-factor, an analytical approach was carried out. The overall procedure for the analytical study was based on the following steps:

1) Evaluation of an area of the cracked conductor at different crack extensions;
2) Evaluation of the cracked conductor's moment of inertia;
3) Determination of the position of the neutral axis (NA) for the cracked conductor;
4) Estimation of the moment of inertia of the combined system (cracked conductor/casing pipes);
5) Determination of the position of the NA of the combined system;
6) Assessment of the updated distance from the crack;
7) Stress assessment in the conductor at the crack level;
8) Evaluation of stress intensity factors for different crack extensions.

The Roark's Formulas [26] were used to calculate the second moment of inertia of the cracked conductor. The area and distances from the centroid to extremities can be calculated using the following formulae for a sector of the hollow circle (Fig. 23):

$$A = \alpha t(2R - t) \tag{10}$$

$$y_{c1} = R\left[1 - \frac{2\sin\alpha}{3\alpha}\left(1 - \frac{t}{R} + \frac{1}{2 - t/R}\right)\right] \tag{11}$$

$$y_{c1} = R\left[\frac{2\sin\alpha}{3\alpha(2 - t/R)} + \left(1 - \frac{t}{R}\right)\left(\frac{2\sin\alpha - 3\alpha\cos\alpha}{3\alpha}\right)\right] \tag{12}$$

$$x_{c1} = R\sin\alpha \tag{13}$$

All the terms present in the previous expressions are explained in Fig. 23.

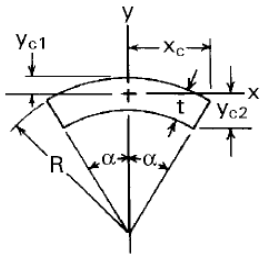

Figure 23: Sector of hollow circle [26].

The moment of inertia about the central axis X for different values of angle α is given by the following expression:

$$I_x = R^3 t\left[\left(1 - \frac{3t}{2R} + \frac{t^2}{R^2} + \frac{t^3}{4R^3}\right) \times \left(\alpha - \sin\alpha\cos\alpha - \frac{2\sin^2\alpha}{\alpha}\right) + \frac{t^2\sin^2\alpha}{3R^2\alpha(2 - t/R)}\left(1 - \frac{t}{R} + \frac{t^2}{6R^2}\right)\right]$$

The analytically determined stress intensity factors (related to the bending stress of 1 MPa applied on the external surface of the conductor) were plotted versus the crack position α. The respective curve in Fig. 24 shows a very close agreement between the values of the *inversion* angles, calculated with FE analyses (nearly 85°) and analytical analysis (nearly 82°).

Stage 3

The crack-propagation analysis at Stage-3 was carried out when the crack in the conductor pipe was prevented to grow further because its crack front reached the compression zone. The FE mesh of the model at the end of Stage 2 (after crack in the conductor pipe reached *TW5)* was modified as illustrated in Fig. 25, and the crack-propagation analysis started until the crack propagating in the casing pipe through its thickness became a through-the-thickness crack. In this case, the residual ligament in the conductor was deemed to remain of constant size throughout the simulation.

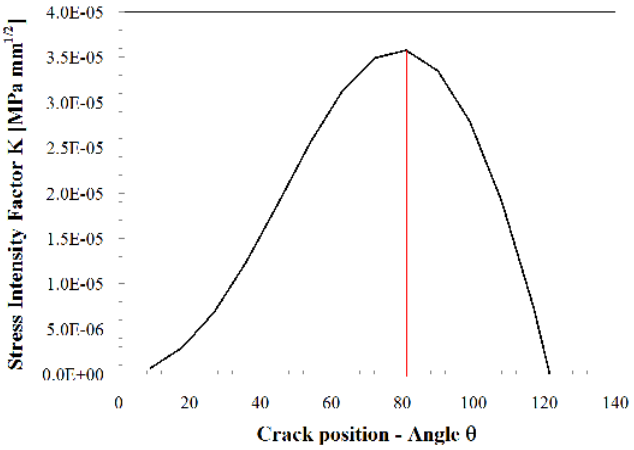

Figure 24: Analytical solution for K (bending stress 1 MPa).

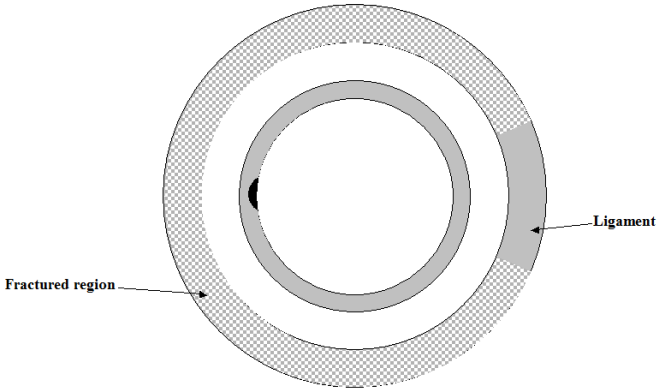

Figure 25: Stage-3 crack configuration.

In Fig. 26 the profile of the inside-wall crack growing through the thickness in the casing pipe (while no further crack growth happens in the Conductor pipe) is presented.

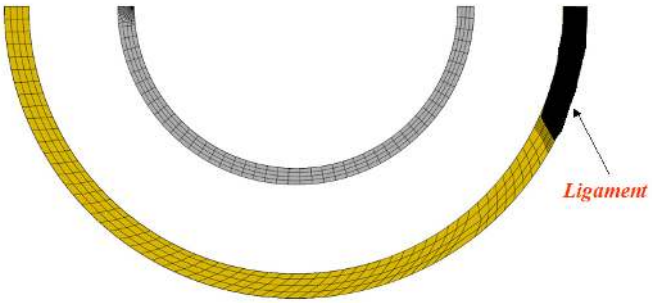

Figure 26: Detail of residual ligament in conductor.

Stage 3: Numerical results

The number of cycles necessary for the thickness node to reach the external surface of the casing and the effect of crack depth on the stress intensity factor are presented respectively in Figs. 27 and 28.

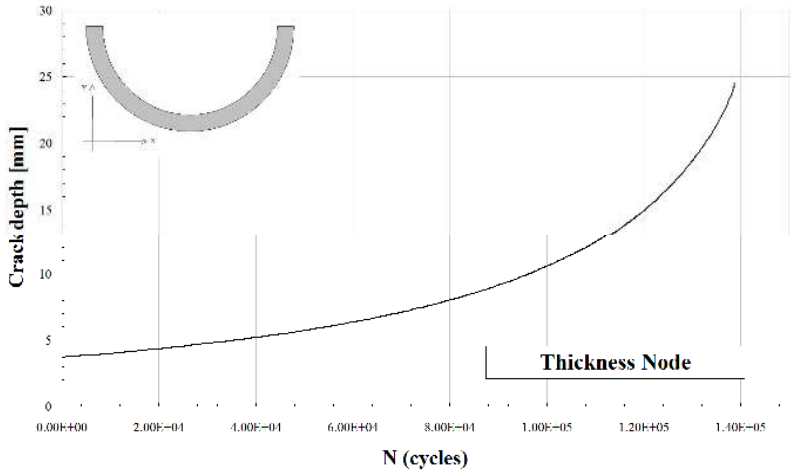

Figure 27: Number of cycles to achieve through-the-thickness crack in casing.

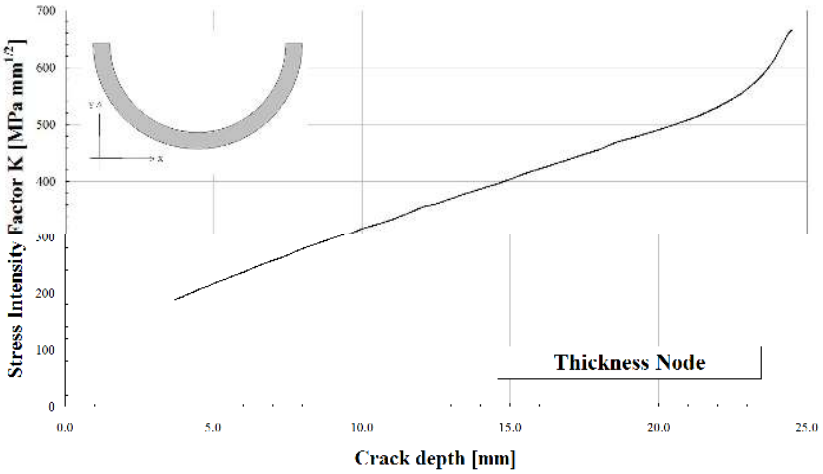

Figure 28: Stress intensity factor *vs.* crack depth (casing).

In Fig. 28, it is interesting to notice that the magnitude of K values is now comparable to the calculated values of K for the previously investigated configurations. This behaviour clearly demonstrates that the casing bears most of the bending load.

EFFECT OF LOADING

In order to achieve a full understanding of the mechanical behaviour of the Subsea Wellhead System in presence of flaws and to develop the most effective damage-tolerant design, five representative scenarios were investigated under variable loading conditions. In particular, the maximum stresses in the range from 80 MPa to 200 MPa were applied. These further analyses gave the possibility to understand the effect of different bending moments on damage tolerance capability of five full-system configurations. The examined five scenarios are presented in Tab. 10.

Bending moment and fatigue life cycles assessment

The fatigue life, related to the five scenarios, was calculated for stress of 80 MPa evaluated on the outside surface of the uncracked conductor pipe. A similar exercise was also carried out for stress of 200 MPa. The fatigue cycles for each of the scenarios and their combinations are shown in Tab. 11 and plotted in Fig. 29. As expected, the maximum fatigue life is achieved for Scenario 2. In this case, the conductor pipe remained intact and a relatively reduced load was borne by the casing pipe. A more realistic fatigue life for the system was obtained when considering a combination of scenarios 1, 3 and 5. In Scenario 1, the inner wall crack in the conductor pipe grew into a through-the-thickness crack first and then, as

shown in Scenario 3, this crack propagated circumferentially in the conductor until it stabilised thanks to the compressive stress state established in the remaining ligament of the pipe due to the shifting neutral axis. At that stage, the inner-wall crack in the casing pipe started growing until it became a through crack, as shown in Scenario 5.

Scenario	*Scenario description*	*Scenario presentation*
1	Semi-circular crack only in conductor pipe	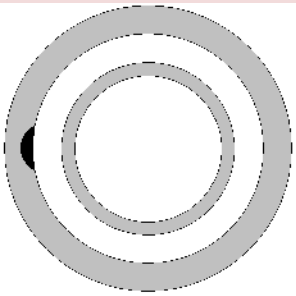
2	Semi-circular crack only in casing pipe	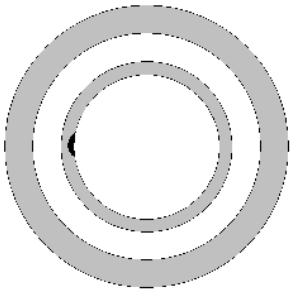
3	Through-the-thickness crack propagating in conductor pipe and semi-circular crack in casing pipe	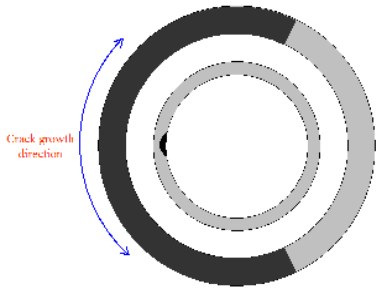
4	Crack propagation only in casing pipe. Conductor is considered fully failed and not bearing any load	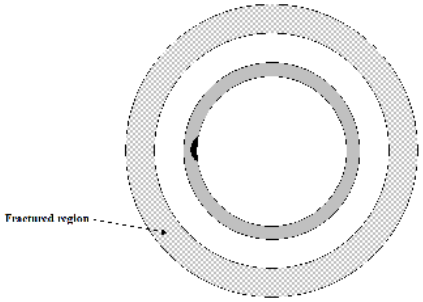
5	Crack propagating only in casing pipe. Crack in conductor is not growing due to compressive stress	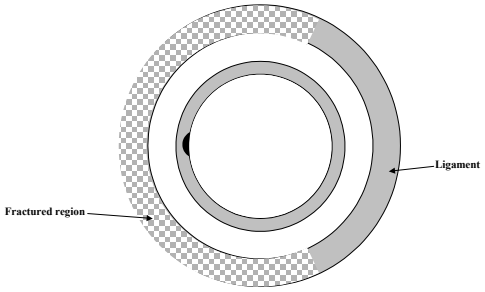

Table 10: Studied scenarios.

Scenario	*Fatigue life (in cycles)* (N)	
	Stress 80 MPa	Stress 200 MPa
1	2.600E+06	1.664E+05
2	1.332E+07	8.525E+05
3	1.907E+05	1.220E+04
4	2.940E+04	1.882E+03
5	1.388E+05	8.883E+03
1 + 3	2.791E+06	1.786E+05
1 + 3 + 4	2.820E+06	1.805E+05
1 + 3 + 5	2.930E+06	1.875E+05

Table 11: Fatigue life for different scenarios.

Once the casing-pipe crack became a through crack, the entire pressure barrier provided by the casing pipe disappeared. In the graph (Fig. 29), each line represents the fatigue life of the pipe-in-pipe system for a particular damaging condition for different cyclic-loading combinations. It can be clearly seen that the majority of the fatigue life is borne by the conductor pipe (Scenario 1), whereas the fatigue life represented by Scenario 2 is rather unlikely. All the other combinations are between Scenarios 1 and 2.

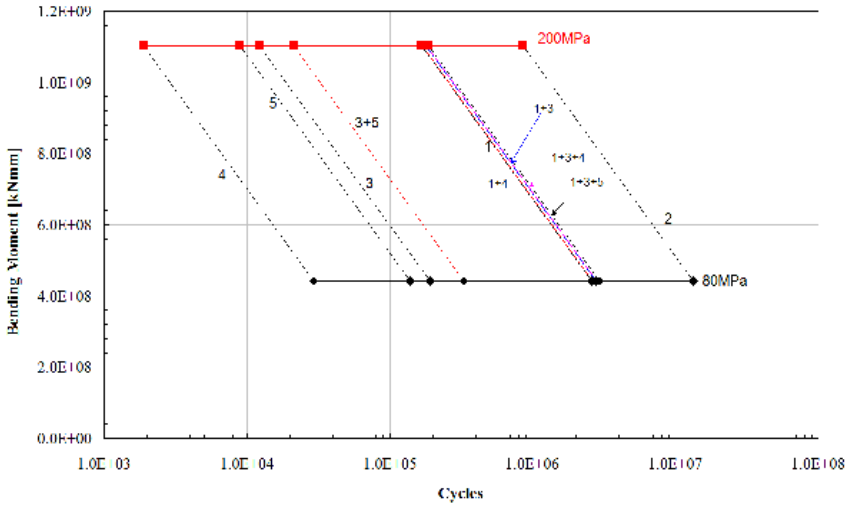

Figure 29: Bending moment (amplitude) vs. fatigue life for various scenarios

Of paramount importance is the magnitude of the bending stress, which may lead to reaching the critical stress intensity factor. Based on fracture mechanics, the fatigue life of a component is reached when the value of the stress intensity factor exceeds the material's critical fracture strength K_c causing the component failure. Stress intensity factors K on the inner surface as the through crack propagates around the conductor (Scenario 3), are plotted as a function of loading cycles in Fig 30. The lowest curve corresponds to the load level applied in the analysis, and shows that the K value does not exceed K_c (which is 7190 MPa mm$^{1/2}$). The *K-N* response was studied for the levels of bending moment multiplied by factors of 2.5, 3, 4 and 5 to generate additional curves in Fig. 30. The scale factor *2.5* gives a peak K close to K_c. Higher scaling values give K values above K_c. Only for comparison purposes, the analyses exceeding K_c value were not prevented to complete the full crack growth simulation, albeit the critical stress intensity value was already reached.

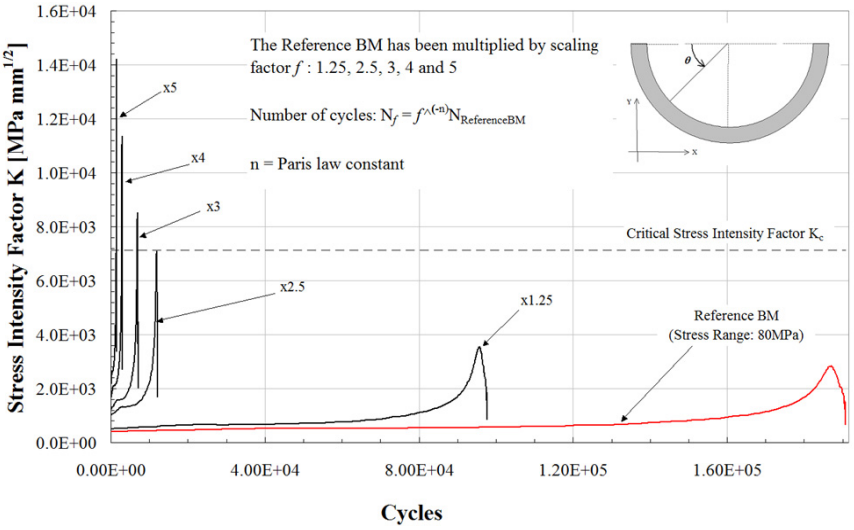

Figure 30: Variation of K with cycles for different load cases .

CONCLUSION

An analytical and numerical study based on the LEFM theory was carried out for the girth weld (although the weld was not explicitly modelled) of the subsea wellhead system. Analytical studies were performed either to establish necessary parameters (e.g. initial crack dimensions) or to validate the finite-element results. The combined study allowed a thorough assessment of the overall behaviour of the wellhead system under cyclic loading conditions for different flaw extensions and various stress ranges. It was demonstrated that most of the load was borne by the conductor pipe even for relatively extended flaws while the crack in the casing pipe underwent a virtually negligible crack growth in the fully coupled system with a kinematic constraint. Furthermore, this study allowed the evaluation of an adequate modelling strategy (e.g. kinematic coupling), which will help pipeline engineers to assess accurately structures with flaws and, in particular, compound systems. The effect of welding residual stress [27, 28] is also important for subsea wellhead systems, especially for low-toughness steels, where a high tensile residual stress can provide a significant part of the crack driving force. Therefore, although this study proposed an efficient approach to the structural integrity assessment of subsea wellhead systems, the future work will contemplate the direct modelling of girth welds and the effect of residual stresses, induced during the welding process, on crack initiation and propagation.

REFERENCES

[1] DNV-RP-C203, Fatigue design of offshore steel structures, Det Norske Veritas (2005).
[2] Robelius, F., Giant oil fields-the highway to oil: Giant oil fields and their importance for future oil production, PhD thesis, Uppsala University, (2007).
[3] King Lim, T., Tellier, E., Howells, H., Wellhead, Conductor and Casing Fatigue-Causes and Mitigation, In: Deep Offshore Technology (DOT), Perth, Australia, (2012).
[4] Det Norske Veritas, Well Fatigue Analysis Method, Report for JIP Structural Well Integrity, Report No. 2011-0063, Revision 01, (2011).
[5] Evans, J., An Evaluation of the Fatigue Performance of Subsea Wellhead Systems and Recommendations for Fatigue Enhancements, In: Offshore Technology Conference (OTC), Houston, USA, (2011).
[6] Buitrago, J., Baxter, D., Hudak S., High-cycle and low-cycle fatigue resistance of girth welds in sour service, In: Proceedings of 27th International Conference on Offshore Mechanics and Arctic Engineering, Estoril, Portugal, (2008) 57545.
[7] Chen, X., Qiao, G., Han, X., Wang, X., Xiao, F., Liao, B., Effects of Mo, Cr and Nb on microstructure and mechanical properties of heat affected zone for Nb-bearing X80 pipeline steels, Materials and Design, 53 (2014) 888–901.

[8] Bordbar, S., Alizadeh, M., Hojjat Hashemi, S., Effects of microstructure alteration on corrosion behavior of welded joint in API X70 pipeline steel, Materials and Design, 45 (2013) 597–604.
[9] Zheng, S.H., Wu, Q.S., Huang, Q.Y., Liu, S.J., Han, Y.Y., Influence of different cooling rates on the microstructure of the HAZ and welding CCT diagram of CLAM steel, Fusion Engineering and Design, 86 (2011) 2616-2619.
[10] Kong, J., Zhen, L., Guo, B., Li, P.H., Influence of Mo content on microstructure and mechanical properties of high strength pipeline steel, Materials and Design, 25 (2004) 723–728.
[11] Moeinifar, S., Kokabi, A.H., Madaah Hosseini, H.R., Influence of peak temperature during simulation and real thermal cycles on microstructure and fracture properties of the reheated zones, Materials and Design, 31 (2010) 2948–2955.
[12] El-Danaf, E., Baig, M., Almajid, A., Alshalfan, W., Al-Mojil, M., Al-Shahrani, S., Mechanical, microstructure and texture characterization of API X65 steel, Materials and Design, 47 (2013) 529–538.
[13] Moeinifar, S., Kokabi, AH., Madaah Hosseini, H.R., Effect of tandem submerged arc welding process and parameters of Gleeble simulator thermal cycles on properties of the intercritically reheated heat affected zone, Materials and Design, 32 (2011) 869–876.
[14] Liu, P., Zheng, J., Zhang, B., Shi, P., Failure analysis of natural gas buried X65 steel pipeline under deflection load using finite element method, Materials and Design, 31 (2010) 1384–1391.
[15] Ghajar, R., Mirone, G., Keshavarz, A., Ductile failure of X100 pipeline steel – experiments and fractography, Materials and Design, 43 (2013) 513–25.
[16] Maligno, A.R., Rajaratnam, S., Leen, S., Williams, E., A three-dimensional (3D) numerical study on fatigue crack growth using remeshing techniques, Engineering Fracture Mechanics, 77 (2010) 94-111.
[17] Maligno, A.R., Soutis, C., Silberschmidt, V.V., An advanced numerical tool to study fatigue crack propagation in aluminum plates repaired with a composite patch, Engineering Fracture Mechanics, (2013) 62-78.
[18] BS 7910, Guide to methods for assessing the acceptability of flaws in metallic structures, British Standards Institution, London (2005).
[19] BS 7608, Code of practice for Fatigue design and assessment of steel structures, British Standards Institution, London (1993).
[20] Abaqus Reference Manual - Abaqus version 6.12.
[21] Citarella, R., Cricrì, G., Comparison of DBEM and FEM Crack Path Predictions in a notched Shaft under Torsion, Engineering Fracture Mechanics, 77 (2010) 1730-1749.
[22] Citarella, R., Cricrì, G., Lepore, M., Perrella, M., DBEM and FEM Analysis of an Extrusion Press Fatigue Failure. In: A. Öchsner, L.F.M. da Silva, H. Altenbach (eds.), Materials with Complex Behaviour – Advanced Structured Materials, 3 (2) (2010) 181-191, DOI:10.1007/978-3-642-12667-3_12.
[23] Al Laham, S., Stress Intensity Factor and Limit Load Handbook, British Energy Generation Ltd, EPD/GEN/REP/0316/98 ISSUE 2.
[24] Rahman, S., Wilkowski, G., Net-section-collapse analysis of circumferentially cracked cylinders - Part I: arbitrary-shaped cracks and generalized equations, Engineering Fracture Mechanics, 61 (1998) 191-211.
[25] Rahman, S., Wilkowski, G., Net-section-collapse analysis of circumferentially cracked cylinders - Part II: idealised-shaped cracks and closed form solution, Engineering Fracture Mechanics, 61 (1998) 213-230.
[26] Young, W.C., Budynas, R. G., Roark's Formulas for Stress and Strain, McGraw-Hill, Seventh Edition (2002).
[27] Armentani, E., Pozzi, A., Sepe, R., Finite-element simulation of temperature fields and residual stresses in butt welded joints and comparison with experimental measurements, In: Proceedings of 12th Biennial ASME Conference on Engineering Systems Design and Analysis ESDA2014, (2014).
[28] Sepe, R., Armentani, E., Lamanna, G., Caputo, F., Evaluation by FEM of the influence of the preheating and post-heating treatments on residual stresses in welding, Key Engineering Materials, 627 (2015) 93-96.